

# Fast 2.5D and 3D inversion of transient electromagnetic surveys using the octree-based finite-element method

Longying Xiao<sup>1</sup>, Gianluca Fiandaca<sup>2</sup>, Bo Zhang<sup>3</sup>, Esben Auken<sup>4</sup>, and Anders Vest Christiansen<sup>5</sup>

## ABSTRACT

Two efficient implementations of 3D and 2.5D modeling and inversion are presented to be applicable to large-scale transient electromagnetic (TEM) method explorations. The key novel features are (1) forward response and Jacobian calculations are implemented using the octree-based finite-element method, (2) a mirror approach is used to build a 2.5D inversion scheme for further efficiency, and (3) a flexible link between the forward mesh and inversion model is applied on 3D and 2.5D schemes based on the voxel formulation. We compare the performance of the new implementations with 3D modeling using tetrahedral meshes, with respect to speed and memory requirements. The 3D octree algorithm requires less than 1/3 of the computational time compared with a 3D tetrahedral scheme for equivalent accuracy. The 2.5D octree algorithm further speeds up the process by reducing the computational time by another factor of two.

The inversion uses the Levenberg-Marquart approach minimizing the least-squares criterion of the objective function. We determine the utility of our inversion approach on a synthetic example and a field example. In the synthetic example, the 3D octree inversion result finds superior resolution of a 3D anomaly compared with a 1D result, whereas the 2.5D inversion result is, expectedly, between the 1D and 3D results, but with favorable computational expenses compared with the full 3D solution. The field data set contains 200 soundings, and we perform a 3D inversion on the full survey. A 24-sounding section is then selected for the 2.5D inversion. The 2.5D inversion result finds resistivity features similar to the 3D inversion result at the selected profile. Hence, we conclude that the presented implementations are capable of handling relatively large TEM surveys on modern computational platforms. This could be smaller subsets of production-size surveys where 2D and 3D effects are pronounced.

## INTRODUCTION

Over the past few decades, transient electromagnetic (TEM) modeling and inversion have developed significantly (Auken et al., 2017), supplemented by a continued improvement in instrumentation and a steady growth in computing capabilities. The common industry routine for TEM inversion is to perform either unconstrained layered inversions (Brodie and Fisher, 2008) or constrained 1D inversions (Auken and Christiansen, 2004; Viezzoli et al., 2008; Vignoli et al., 2015). In addition, various forms of rapid approximations (Fullagar et al., 2015; Christensen, 2016) or combinations with accurate and approximate solutions (Christiansen et al., 2016)

often are used. The constrained solutions provide a spatially smooth model, whereas the inherent limitations in the 1D assumption make it challenging or impossible for them to accurately describe complex 2D or 3D geologic structures. These heterogeneities increase the complexity of eddy current patterns, which are commonly found in natural circumstances making a 1D assumption nonapplicable in cases such as mineral exploration (Yang and Oldenburg, 2012) and even in complicated aquifer structures (Maurya et al., 2020). In the last two decades, various numerical 3D TEM modeling algorithms have been presented using the integral equation method (Zhdanov et al., 2006), the finite-difference method (Commer et al., 2015), the finite-volume (FV) method (Haber et al., 2002), and the finite-

Manuscript received by the Editor 24 June 2021; revised manuscript received 14 October 2021; published ahead of production 4 May 2022; published online 20 June 2022.

<sup>1</sup>Formerly Aarhus University, HydroGeophysics Group, Department of Geoscience, Aarhus, Denmark; presently Geological Survey of Finland, Espoo, Finland. E-mail: longying.xiao@gtk.fi.

<sup>2</sup>University of Milano, Department of Earth Sciences “Ardito Desio,” Milano, Lombardia, Italy. E-mail: gianluca.fiandaca@unimi.it.

<sup>3</sup>Jilin University, College of Geo-exploration Sciences and Technology, Changchun, China. E-mail: em\_zhangbo@163.com (corresponding author).

<sup>4</sup>Geological Survey of Denmark and Greenland, Copenhagen, Denmark. E-mail: ea@geus.dk.

<sup>5</sup>Aarhus University, HydroGeophysics Group, Department of Geoscience, Aarhus, Denmark. E-mail: anders.vest@geo.au.dk.

© 2022 Society of Exploration Geophysicists. All rights reserved.

element (FE) method (Um et al., 2010). The 3D inversion of TEM data is a massive computational challenge. First, the time-domain data from one receiver contain tens of time gates spanning several decades in time, and the forward problems need to be solved twice for each iteration during the inversion, one time for the forward and the other for the Jacobian. Second, hundreds of thousands of TEM soundings are commonly collected in one survey. In recent years, several strategies are reported in the literature to solve the 3D TEM inversion problem more effectively. Cox et al. (2012) introduce the “footprint” concept in the time-domain data, in which only elements close to the system with significant data impact are considered for sensitivity calculation; Oldenburg et al. (2013) demonstrate that the performance of direct solvers outruns traditional iterative solvers; and Yang et al. (2013) use local meshes to decompose the inversion domain into small problems. Even so, it remains a computationally expensive task to realize a large-scale multidimensional time-domain inversion for TEM surveys. Here, we present a 3D inversion scheme and a 2.5D inversion scheme through octree FE modeling and a multimesh approach, which decomposes the survey domain using a local mesh at each sounding for forward calculation and a full-survey model mesh for inversion. We will refer to this strategy as the domain decomposition.

The computation of the TEM forward response and Jacobian calculation accounts for the bulk of the computational cost in a 2D and 3D inversion scheme, and we, therefore, seek to achieve computational savings on this process through nonuniform meshing. Local refinement only applied in the regions where fine resolution is needed to represent complex geometry features and capture large field variations, such as areas close to the transmitter and receiver or places including a conductivity discontinuity, can effectively reduce the number of unknowns in the linear system to be solved (Horesh and Haber, 2011). Compared with unstructured grids adopted to 3D electromagnetic (EM) modeling programs using either the FE method (Schwarzach et al., 2011; Um, 2011; Ansari and Farquharson, 2014) or the FV solution (Jahandari and Farquharson, 2014), octree meshes are easier to construct, the resulting system often is better conditioned, and the number of cells remains reasonable for numerical computation (McMillan et al., 2018). The earliest application in the EM field using octree meshes was done by Haber and Heldmann (2007), who demonstrate the advantage of octree discretization using the FV solution for Maxwell’s equations. Grayver and Kolev (2015) also show that considerable computational savings can be achieved on magnetotelluric inversion problems. Haber and Schwarzach (2014) use an FV solution for TEM on octree meshes, but to our knowledge, there is no TEM inversion solution using octree meshes with the FE method. Furthermore, we have not, so far, seen any direct performance comparison over different implementations using different nonuniform meshes. We, therefore, present two octree-based solutions and a performance comparison with a tetrahedral-based solution in this paper.

The 2.5D inversion was once a preferred solution when available computational power was smaller than today (Allers et al., 1994; Mitsuhashi et al., 2002) and was challenging to complete a 3D inversion for multiple soundings, especially for time-domain data sets. Traditionally, the 2.5D algorithms were based on the 2.5D formulations of Maxwell’s equations (Wilson et al., 2006; Abubakar et al., 2008; Yu and Haber, 2012), which compute the response of a 3D source from a 2D geoelectric model using different numerical methods. In this study, we followed a different approach, easily

generalized to any problem in which the 3D solution is available. Specifically, we developed a 2.5D algorithm based on a 3D modeling mesh halved through the 2D  $xz$ -plane passing through the receiver and transmitter (i.e., along the moving direction for towed or airborne systems). Assumptions on the symmetry of the modeling, in terms of source and boundary conditions, allow us to almost halve the degrees of freedom (DoF) in the linear system for forward responses and Jacobian calculations, and thereby achieve a factor of two speed-up in our 2.5D inversion compared with the complete 3D solution.

Decoupling between the modeling mesh and inversion mesh combined with the domain decomposition strategy offers flexibility to design a local modeling mesh for each sounding and a regional inversion mesh for the survey. Madsen et al. (2020) use two separate meshes for forward modeling and inversion to solve the direct current and induced polarization problem. Zhang et al. (2021) also apply this decoupling method and use two tetrahedral meshes with different densities for forward modeling and Jacobian calculation to accelerate a 3D TEM inversion. In this study, we apply the decoupling of the inversion mesh and the forward modeling mesh to octree-based forward modeling. This enables the utilization of a regular inversion model grid while maintaining the advantages of the nonuniform nature of the octree mesh in the forward modeling.

The goal of this paper is to present two highly efficient TEM inversion schemes that can be applied to any TEM system, airborne, land-based, or on water. The inversion schemes are using the octree-based FE method for forward modeling with the second-order backward Euler method (Butcher and Goodwin, 2008): the multimesh approach with the domain decomposition for inversion and a mirror approach for the 2.5D inversion. In the next section, we describe the FE discretization using octree meshes for the TEM forward and Jacobian calculation, and include a brief description of our inversion scheme. Then, we verify the effectiveness of the algorithm through two numerical experiments using the towed transient electromagnetic (tTEM) system (Auken et al., 2019). The first example presents 3D and 2.5D forward responses of resistive and conductive half-space models against 1D responses. Following this, we present a performance analysis comparing against 3D tetrahedral results. The second example shows the synthetic inversion results of a 3D valley model from 1D, 2.5D, and 3D algorithms. Finally, we present inversions of field data that demonstrate the advantages of our approaches.

## METHODOLOGY

### Forward modeling

#### Forward problem formulation

Assuming that the medium is linear, isotropic, and homogeneous and that the electrical properties are independent of time, pressure, and temperature, the time-domain forward problem follows the derivation from quasi-static Maxwell’s equations and can be formulated as a diffusion equation in terms of the electrical field as a function of space  $\mathbf{r}$  and time  $t$ , i.e.,  $\mathbf{e}(\mathbf{r}, t)$ :

$$\nabla \times \nabla \times \mathbf{e}(\mathbf{r}, t) + \mu\sigma(\mathbf{r}) \frac{\partial \mathbf{e}(\mathbf{r}, t)}{\partial t} = -\frac{\partial \mathbf{j}_s(t)}{\partial t}, \quad (1)$$

where  $\mathbf{r} \in \Omega$ ,  $t \in (0, T)$ ,  $\mathbf{j}_s$  is the electric current density,  $\sigma$  is the electric conductivity, and  $\mu$  is the magnetic permeability. The initial conditions are given as



hanging nodes on the faces (Grayver, 2015), which require special treatment when we compose the system matrix.

We need to handle the added parameters from the edges associated with hanging nodes, to ensure the compatibility of the FE approximation and the continuity of the FE fields even on the interface. Our solution is inspired by the work of Bielak et al. (2005), who select the added parameters and treat them using a properly weighted constraint during the stiffness matrix assembly process in equation 7.

Based on the classic FE solution  $\mathbf{e}$  as in equation 5, the field definition in the octree-based FE is extended as

$$\mathbf{e} = \sum_{i_1=1}^{12-n_h} \mathbf{N}_{i_1} e_{i_1} + \sum_{i_2=1}^{n_h} \mathbf{N}_{i_2} \left( \sum_{j=1}^{n_{ed}} d_j^{i_2} \cdot \phi_j^{i_2} \right), \quad (14)$$

where  $n_h$  represents the number of edges with hanging nodes,  $d_j^{i_2}$  are fields on the edges of lower-level master cells that are associated with the added parameters,  $\phi_j^{i_2}$  denotes the enrichment function applied on the added parameters, and  $n_{ed}$  is the number of related edges. Given that the property of the edge element and all of the elements are regular, we define the enrichment function as

$$\phi_j^{i_2} = \begin{cases} 1 & \text{on the edge, } n_{ed} = 1 \\ (1/2, 1/2) & \text{on the face, } n_{ed} = 2 \end{cases}. \quad (15)$$

Note that, when the hanging node is on the face, two parallel edges on the face share the contribution equally, as the field varies linearly in the normal direction to the vector. In general, the main idea of our approach is to redefine the shape function of edges at the hanging nodes by linear combinations of the previous shape functions, similarly to Grayver (2015).

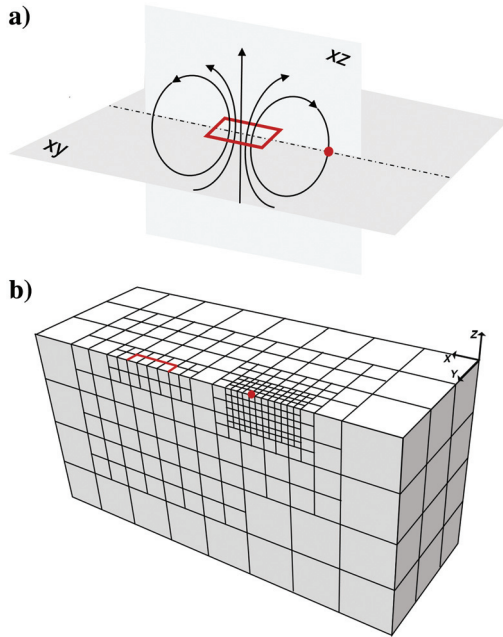


Figure 2. Mirror approach illustration, where the red rectangle symbolizes the transmitter of the tTEM system (the size of the transmitter is 4 m × 2 m) and the red dot symbolizes a dipole receiver. (a) The magnetic field on the bisector plane and (b) octree forward mesh in the 2.5D inversion.

Therefore, the fields at the edges associated with hanging nodes can be expressed by the edges from master cells, and the dimension size of the stiffness matrix is always smaller than the number of physical edges.

### 2.5D solution: The mirror approach

During a TEM survey, it is common that the transmitter, either in offset configuration or in a central loop configuration, is geometrically symmetric. Here, we take the tTEM system (Auken et al., 2019) as an example to illustrate the principle of the mirror approach, which is the base of our 2.5D implementation. We assume that the resistivity model has variations in the  $x$ - and  $z$ -directions and is symmetric in the  $y$ -direction. The  $x$ -direction is defined by a line passing through the center of the transmitter and the receiver. In this condition, the magnetic fields on the  $xy$ -plane are symmetric, with values mirrored from the left side to the right side of the  $xz$ -plane, and they have no  $y$  component along the  $xz$ -plane, because of the system and 2D model symmetry. No  $y$  component of the magnetic field in the  $xz$ -plane means that the electric field has zero  $x$  and  $z$  components on the plane, because of Faraday's law. These are exactly the Dirichlet boundary condition that we set in the 3D modeling on the outer faces of the forward mesh.

Consequently, if we remove a flank of the original 3D model according to the bisector of the system (see Figure 2) as well as the transmitter, and we apply the Dirichlet boundary condition on all mesh outer faces including the mirroring  $xz$ -plane, we will obtain a forward modeling equivalent to the full problem in which the resistivity is defined in the entire mesh, left and right of the  $xz$ -plane mirroring plane. By defining the model in the half mesh and using a resistivity model in the half mesh that does not change along the  $y$ -direction, we obtain a pseudo-2.5D solution to the problem, using a 3D implementation with proper source definition and boundary conditions.

An analogous point of view is the one that looks at the stiffness matrix of the problem. If we take equation 6 with a size of 4 × 4 matrix (four unknowns) as an example, the original 3D system matrix would be

$$\begin{aligned} K_{11}e_1 + K_{12}e_2 + K_{13}e_3 + K_{14}e_4 &= b_1, \\ K_{21}e_1 + K_{22}e_2 + K_{23}e_3 + K_{24}e_4 &= b_2, \\ K_{31}e_1 + K_{32}e_2 + K_{33}e_3 + K_{34}e_4 &= b_3, \\ K_{41}e_1 + K_{42}e_2 + K_{43}e_3 + K_{44}e_4 &= b_4. \end{aligned} \quad (16)$$

With the symmetric conditions of the fields and the information of cells from the mirror approach, namely,

$$e_1 = e_2,$$

$$e_3 = e_4,$$

$$K_{i1} = K_{i2}, (i \in 1, 4),$$

$$K_{i3} = K_{i4}, (i \in 1, 4), \quad (17)$$

then equation 16 in the half mesh will be

$$K_{11}e_1 + K_{13}e_3 = b_1/2,$$

$$K_{21}e_1 + K_{23}e_3 = b_2/2. \quad (18)$$

In this manner, half of the cells can be saved from computation without the accuracy being affected. To achieve this, we need to use only half of the transmitter as the source input because the entire system still follows the same physical law on half of the 3D forward mesh. Consequently, this is de facto mathematical optimization, where the 2.5D problem is characterized as a 3D source on a mirrored model using a 3D octree mesh.

### Jacobian calculation

The Jacobian is the matrix of sensitivities with size  $N_d$  (the number of data) by  $N_e$  (the number of elements), and each element in the matrix reflects the contribution to the response of conductivity at this point (Christensen, 2014). We calculate the Jacobian in an explicit backward stepping scheme (Börner, 2010) through adjoint forward modeling. This methodology is applied to the 3D and 2.5D inversion because we calculate the Jacobian in the octree mesh first and then interpolate to the inversion model mesh, as illustrated in Figure 3.

Let us define the Jacobian matrix for each step  $n$  as

$$\mathbf{J}^n = \frac{\partial \mathbf{d}_{\text{sys}}^n}{\partial \mathbf{m}} \quad (19)$$

The derivative of equation 6 with respect to model parameters  $\mathbf{m}$  will be

$$\frac{\partial \mathbf{e}}{\partial \mathbf{m}} = \mathbf{K}^{-1} \mathbf{G}, \quad (20)$$

where

$$\mathbf{G} = -\frac{\partial \mathbf{K}}{\partial \mathbf{m}} \mathbf{e}. \quad (21)$$

Combing the interpolation matrix  $\mathbf{L}$  in equation 13, the Jacobian matrix is derived as

$$\mathbf{J}^T = \mathbf{G}^T \mathbf{K}^{-T} \mathbf{L}^T. \quad (22)$$

If we define a vector  $\mathbf{V} = \mathbf{K}^{-T} \mathbf{L}^T$ , then we have the adjoint modeling equation:

$$\mathbf{K}^T \mathbf{V} = \mathbf{L}^T. \quad (23)$$

Solving equation 23 through the backward propagation from the last time step, we have the temporary vector  $\mathbf{V}$ . We thus obtain the Jacobian through the relation

$$\mathbf{J}^T = \mathbf{G}^T \mathbf{V}. \quad (24)$$

### Multimesh approach

The definition of model parameters and forward meshes is obtained by adapting the approach of Christensen et al. (2017) and Madsen et al. (2020) with domain decomposition. Domain decomposition breaks the full-survey forward prob-

lem into small tasks at the soundings, minimizing the computing expenses without sacrificing modeling accuracy. Specifically, we used two sets of separate octree meshes for forward modeling and Jacobian calculation at each transmitter, in which we compute the forward response from equation 6 and the Jacobian from equation 24 using the adjoint modeling method.

We designed one voxel mesh for the full-scale model update in the inversion, in which the model parameters are defined in two different ways for 3D and 2.5D inversions (see Figure 3). In three dimensions, the parameters are determined on the nodes of a 3D regular structured mesh, with uniform node spacing in the  $x$ - and  $y$ -directions and log-increasing node spacing in the  $z$ -direction. In 2.5D inversions, the parameters are specified on the nodes of 2D sections, which follow the acquisition lines, with uniform node spacing along lines and log-increasing vertical spacing. The inversion model parameters are linked to the center of the forward mesh elements through interpolation with an inverse distance function:

$$\mathbf{m} = f(\mathbf{M}) = \mathbf{F} \cdot \mathbf{M}, \quad (25)$$

where the vector  $\mathbf{m}$  represents the values of model parameters in the forward mesh elements and  $\mathbf{M}$  holds the resistivity values at the voxel nodes in the inversion mesh. Here,  $\mathbf{F}$  is an interpolation matrix with weights, which merely relies on the relative distances between the forward mesh elements with the model nodes used for interpolation.

Because the interpolation function is a linear operation, and applying the chain rule for derivatives, so that

$$\frac{\partial \mathbf{d}}{\partial \mathbf{M}_i} = \sum_j \frac{\partial \mathbf{d}}{\partial \mathbf{m}_j} \frac{\partial \mathbf{m}_j}{\partial \mathbf{M}_i} = \sum_j \frac{\partial \mathbf{d}}{\partial \mathbf{m}_j} F_{j,i}, \quad (26)$$

we, therefore, write the Jacobian on the model mesh mapping from Jacobian mesh as

$$\mathbf{J}_M = \mathbf{J}_m \cdot \mathbf{F}^T, \quad (27)$$

where  $\mathbf{J}_M$  is the Jacobian of the inversion model space, the voxel mesh, and  $\mathbf{J}_m$  is the Jacobian computed in the forward mesh through equation 24.

This multimesh approach, with model parameters defined on the regular meshes and forward/Jacobian computations carried out on

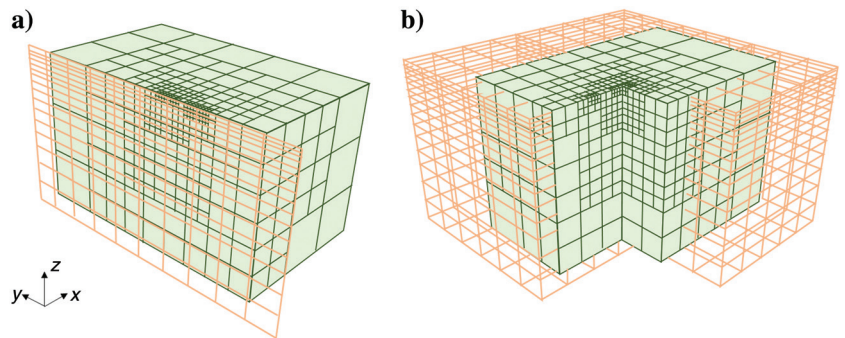


Figure 3. Relation between forward/Jacobian mesh (green) and inversion model mesh (orange). (a) The 2.5D inversion: 3D octree mesh and 2D inversion section. (b) The 3D inversion: 3D octree mesh and 3D inversion mesh.

octree meshes, one for each transmitter, allows for minimizing computation time and resource requirements while maintaining an inversion model space well suited for inversion. In this fashion, enforcing vertical and horizontal constraints for the inversion becomes easily applicable, as well as incorporating other prior knowledge, when present.

## Inversion

For inversion, we adopted the framework from AarhusInv (Auken et al., 2015), which provides means for minimizing a general multicomponent objective function:

$$\mathbf{Q}(\mathbf{m}) = \frac{\mathbf{Q}_{\text{obs}}(\mathbf{m}) + \mathbf{Q}_{\text{prior}}(\mathbf{m}) + \mathbf{Q}_{\text{reg}}(\mathbf{m})}{N_{\text{obs}} + N_{\text{prior}} + N_{\text{reg}}}, \quad (28)$$

where each component of the objective function describes the norm misfit of the solution with respect to the observed data, prior information, and regularizing constraints, respectively ( $N_{\text{obs}}$ ,  $N_{\text{prior}}$ , and  $N_{\text{reg}}$  being the number of data, the number of prior constraints, and the number of roughness constraints).

In our algorithm, the objective function is minimized iteratively following the rules of the Levenberg-Marquardt adaptive minimization scheme (Hanke, 1997; Menke, 2018), which combines the gradient descent method with the Gauss-Newton (GN) method, to obtain the optimal convergence rate. Hence, the  $n + 1$ th iterative model update vector  $\mathbf{m}$  becomes

$$\mathbf{m}_{n+1} = \mathbf{m}_n + [\mathbf{J}'_{(n)} \mathbf{C}'_{(n)-1} \mathbf{J}'_{(n)} + \lambda_{(n)} \mathbf{I}]^{-1} \cdot [\mathbf{J}'_{(n)} \mathbf{C}'_{(n)-1} \delta \mathbf{d}'_{(n)}]. \quad (29)$$

Here, the damping parameter  $\lambda_{(n)}$  is regenerated at each step, which determines the contribution amount of the gradient descent and the GN method on the current iteration by scaling the identity matrix  $\mathbf{I}$ ;  $\mathbf{J}'_{(n)}$  denotes the Jacobian matrix of partial derivatives;  $\delta \mathbf{d}'_{(n)}$  is the data vector update; and  $\mathbf{C}'_{(n)}$  is a covariance matrix:

$$\mathbf{J}'_{(n)} = \begin{bmatrix} \mathbf{J}_{(n)} \\ \mathbf{P} \\ \mathbf{R} \end{bmatrix}, \quad (30)$$

$$\delta \mathbf{d}'_{(n)} = \begin{bmatrix} \delta \mathbf{d}_{(n)} \\ \delta \mathbf{m}_{(n)} \\ \delta \mathbf{r}_{(n)} \end{bmatrix} = \begin{bmatrix} \mathbf{d}_{(n)} - \mathbf{d}_{\text{obs}} \\ \mathbf{m}_{(n)} - \mathbf{m}_{\text{prior}} \\ -\mathbf{R} \mathbf{m}_{(n)} \end{bmatrix}, \quad (31)$$

$$\mathbf{C}'_{(n)} = \begin{bmatrix} \mathbf{C}_{\text{obs}} & 0 & 0 \\ 0 & \mathbf{C}_{\text{prior}} & 0 \\ 0 & 0 & \mathbf{C}_R \end{bmatrix}. \quad (32)$$

In the first equation of the Jacobian matrix (equation 30),  $\mathbf{J}_{(n)}$  thus represents the Jacobian of the forward mapping,  $\mathbf{P}$  is the constraint matrix on the a priori information, and  $\mathbf{R}$  is the roughness matrix. In equation 31, the data vector update  $\delta \mathbf{d}'_{(n)}$  includes the

distance  $\delta \mathbf{d}_{(n)}$  between the  $n$ th forward response  $\mathbf{d}_{(n)}$  and the observed data  $\mathbf{d}_{\text{obs}}$ , the distance  $\delta \mathbf{m}_{(n)}$  between the  $n$ th model update  $\mathbf{m}_{(n)}$  and a priori model vector  $\mathbf{m}_{\text{prior}}$ , and roughness of the  $n$ th model vector  $\delta \mathbf{r}_{(n)} = -\mathbf{R} \mathbf{m}_{(n)}$ . The three blocks of the covariance matrix  $\mathbf{C}'$  contain the covariance on the observed data  $\mathbf{C}_{\text{obs}}$ , the covariance on the a priori information  $\mathbf{C}_{\text{prior}}$ , and the covariance on the roughness constraints  $\mathbf{C}_R$ . One can find more detailed matrix format and derivations in Auken and Christiansen (2004). No prior information was incorporated in the examples of this paper. However, two types of constraints, horizontal and vertical, are enforced, and the roughness matrix  $\mathbf{R}$ , the roughness of the  $n$ th model vector  $\delta \mathbf{r}_{(n)}$ , and the covariance on the roughness constraints  $\mathbf{C}_R$  can therefore be further subdivided into two terms, respectively:

$$\mathbf{R} = \begin{bmatrix} \mathbf{R}_h \\ \mathbf{R}_v \end{bmatrix}, \quad (33)$$

$$\delta \mathbf{r}_{(n)} = \begin{bmatrix} -\mathbf{R}_h \mathbf{m}_{(n)} \\ -\mathbf{R}_v \mathbf{m}_{(n)} \end{bmatrix}, \quad (34)$$

$$\mathbf{C}_R = \begin{bmatrix} \mathbf{C}_{R_h} & 0 \\ 0 & \mathbf{C}_{R_v} \end{bmatrix}. \quad (35)$$

## VERIFICATION

The presented algorithms have been implemented using the programming language Fortran 2003. The mesh generation, forward modeling, and Jacobian calculation are all devised from scratch, which are built into an existing GN inversion scheme (Auken et al., 2015). For solving the system equation 6, we used the solver Pardiso (Schenk and Gärtner, 2004) directly from the Intel Math Kernel Library. To better harness the modern computing architectures and accelerate the process, Open Multi-Processing (OpenMP) was used to perform parallelization over sounding domains. All of the following numerical experiments were run on 2.60 GHz Xeon Gold 6132 central processing unit (CPUs).

### Forward modeling

To demonstrate the effectiveness of our implementations, we conducted a numerical test on a half-space problem, comparing the responses with 1D computations (Auken et al., 2015). The homogeneous half-space model is calculated for resistivities of 10 and 400  $\Omega\text{m}$ , and the air resistivity is defined as  $10^6 \Omega\text{m}$ . The tTEM system, which consists of a 4 m  $\times$  2 m transmitter and a receiver located 9.44 m away from the transmitter loop center, is simulated as shown in Figure 4. We designed the octree mesh to meet a target of 3% accuracy at the receiver position, resulting in a 3D forward mesh with 17,100 DoF and a 2.5D forward mesh with 12,200 DoF. The smallest cell at the receiver is 0.5 m  $\times$  0.5 m  $\times$  0.5 m, whereas the size of the largest cell at the boundary is 1024 m  $\times$  1024 m  $\times$  1024 m. The source waveform was simulated by a linear turn-off of the current from 1 to 5 ns. The responses were compared with the impulse response in the time range from 1 to 10 ms.

Figure 5a illustrates the homogeneous half-space responses with a late time sloping rate of  $-5/2$  for all of the models; Figure 5b

provides a relative error comparison between the octree-based solutions and the 1D solution. The overall relative error is under 3% for all cases, except the early responses of 10  $\Omega\text{m}$  half-space as the solid blue and solid red lines shown, which was caused by the sign change in the early time of the conductive surface. It is possible to achieve an even smaller error margin (less than 1%) as long as the meshing is dense enough to represent tiny field variabilities. However, we deem 3% sufficient when considering the noise level in the production EM data.

### Performance comparison with the tetrahedral implementation

Table 1 presents a comparison, in terms of the running time and memory usage, of the octree 3D and 2.5D implementations and the 3D tetrahedral implementation presented in Zhang et al. (2021). For one local mesh, of which the discretization attains an accuracy of 3% compared with a 1D response, the tetrahedral method requires 40,000 edges, whereas the octree 3D mesh has approximately 17,200 DoF with 27,500 physical edges. The 2.5D mesh yields 12,100 edges, which accounts for 2/3 of the 3D octree mesh. The immediate consequence of the DoF is the computing expense. The 3D octree algorithm requires 20 s for the forward response, which is less than 1/3 of the running time on a 3D tetrahedral scheme. The 2.5D octree algorithm further speeds up the process by reducing the running time by another factor of two. As for memory usage, the 3D octree modeling and Jacobian calculation need 1/3 of the tetrahedral, and 2.5D octree further reduces it to nearly a half of the 3D octree one.

### Synthetic inversions

For synthetic inversions, we designed an idealized 3D model, consisting of a 10  $\Omega\text{m}$  buried valley structure embedded in a 200  $\Omega\text{m}$  homogeneous background. The valley model stretches from 15 to 40 m vertically, with one branch uplifting. It is 130 m wide in the  $y$ -direction, and it extends infinitely in the  $x$ -direction (see Figure 6a). The model was designed such that the valley structure varies horizontally and vertically. In this example, as shown in Figure 6b, we modeled 204 soundings over a 200 m  $\times$  160 m area to cover the valley. The soundings have the interval distance of 20 m in the  $x$ -direction and 10 m in the  $y$ -direction, roughly resembling a typical field data collection.

Each local mesh of 3D or 2.5D inversions had the same size/discretization used in the modeling accuracy example, but contrary to the accuracy example, the tTEM current waveform and system response (Auken et al., 2019) were fully modeled, convolving the impulse response with the waveform and the system filters. This was done for the two system moments, with low-moment times from  $4.14 \times 10^{-6}$  to  $11.6 \times 10^{-5}$  s and high-moment times from  $1.14 \times 10^{-5}$  to  $9.01 \times 10^{-4}$  s, where all timing is referenced against the beginning of the turn-off.

The stopping criterion for all of the inversions is based on the total misfit: the inversion stops when the change in the total misfit of the inversion (equation 28) is smaller than 1%. The same starting model was used as well for all inversions, in this case a homogeneous 100  $\Omega\text{m}$  half-space.

For the 3D modeling and inversion, the line directions of the tTEM systems are all  $x$ -wise,

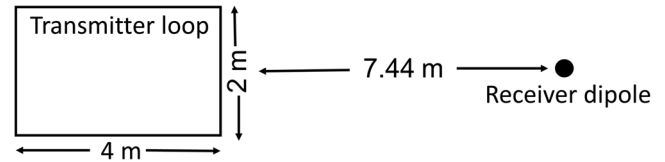


Figure 4. The tTEM system configuration scheme, where the size of the transmitter is 4 m  $\times$  2 m and the dipole receiver locates 9.44 m from the transmitter loop center.

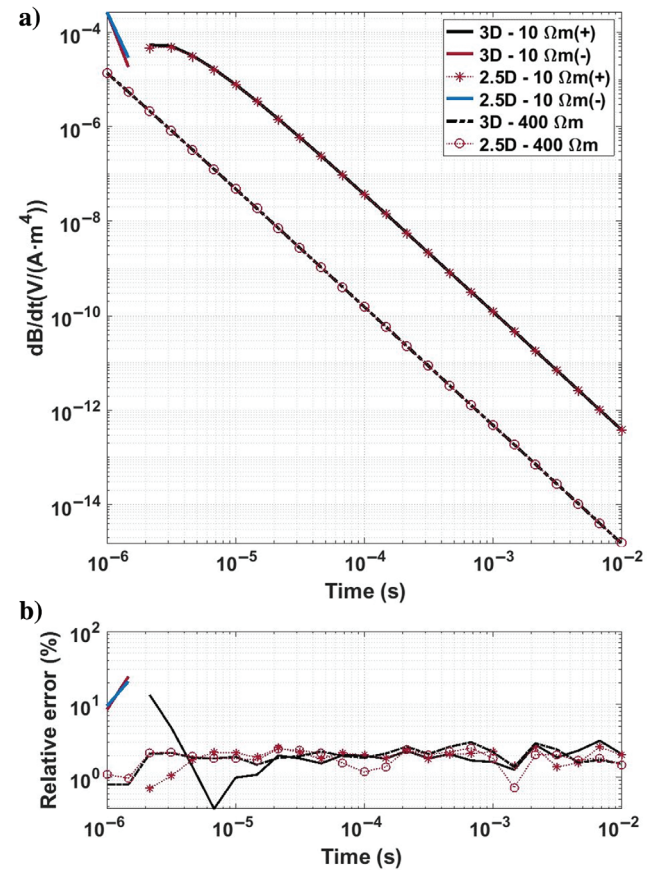


Figure 5. The 2.5D and 3D octree-based hexahedral forward modeling accuracy for a 10/400  $\Omega\text{m}$  half-space model using the tTEM system. (a) Forward responses. (b) The relative difference compared with the corresponding 1D response. Positive and negative responses for the 10  $\Omega\text{m}$  case are shown with different colors, indicated with the signs (+) and (-) in the legend.

**Table 1. Performance and computing costs of forward (Fwd) response and the first iteration (first) for one local mesh.**

	Octree 3D	Tetrahedra 3D	Octree 2.5D
DoF/edge number	17,200/27,500	40,000/40,000	12,100/18,400
Fwd/time (s)	20	72	8
Inv (first)/time (s)	90	374	29
Fwd/memory (MB)	244	678	138
Inv (first)/memory (MB)	615	1300	362

as indicated by A in Figure 6c. It took 13 iterations and 14.8 h on 10 CPUs to complete the 3D inversion, with a final total misfit of 0.60. The peak memory usage for this inversion was 44 GB. A 1D voxel inversion, which used the same model space but 1D forward and Jacobian computations (Christensen et al., 2017), was carried out on the same data for comparison: it took eight iterations and 137 s to end up with a total misfit of 1.06.

Figure 6d and 6e shows an  $xy$  slice at 25 m depth of the 3D and 1D inversion models, respectively. The 1D inversion does not recover the upper branch of the model, but the 3D inversion is able to image both the valley branches, although with poor resolution on the lower branch.

To compare with 2.5D inversion results, we made two profiles, which are illustrated in Figure 6b, where profile A consists of 12 soundings along the  $x$ -direction (at  $y = 130$  m) and profile B consists of 17 soundings along the  $y$ -direction (at  $x = 60$  m). For the 2.5D inversion, it is required that the inversion plane is aligned with the driving direction. Consequently, when generating the data and inverted profile A, the system was assumed driving in the  $x$ -direction, while driving in the  $y$ -direction for profile B, as described in Figure 6c. The sounding layout is the same regardless of the driving direction.

We carried out the 2.5D inversions of profiles A and B and the key inversion numbers are listed in Table 2. The data misfit is calculated as  $\sqrt{Q_{\text{obs}}(\mathbf{m})/N_{\text{obs}}}$ . From the table, we can see that the memory usage increases linearly with the number of soundings. With perfect scaling of the OpenMP parallelization, the running times for one iteration in Table 2 should be identical for profiles

A and B because we used one thread for each sounding. A suboptimal scaling was obtained, with a 20% increase in running time per sounding with 17 threads instead of 12.

Figure 7 presents the synthetic models and 1D, 2.5D, and 3D inversion results along profiles A (left column) and B (right column). Figure 7a shows the model along profile A, with the uplifting branch of the valley that expands 120 m horizontally and from 10 to 35 m in depth. Figure 7b presents an  $xz$  slice of the 3D inversion model of Figure 6, which clearly delineates the shape of the branch, but with an underestimation of resistivity at the bottom of the anomaly. Figure 7c and 7d shows the 2.5D and 1D inversions, respectively. Both inversions have a worse recovery of the anomaly, compared with the 3D inversion. This also is expected for the 2.5D inversion because the anomaly is elongated along the profile direc-

**Table 2. Resources and performance comparisons for 2.5D inversion on profiles A and B.**

	Profile A (12 threads)	Profile B (17 threads)
Peak memory (MB)	4200	6000
Running time, total (s)	871	1342
Iterations	10	13
Data misfit	0.66	0.69

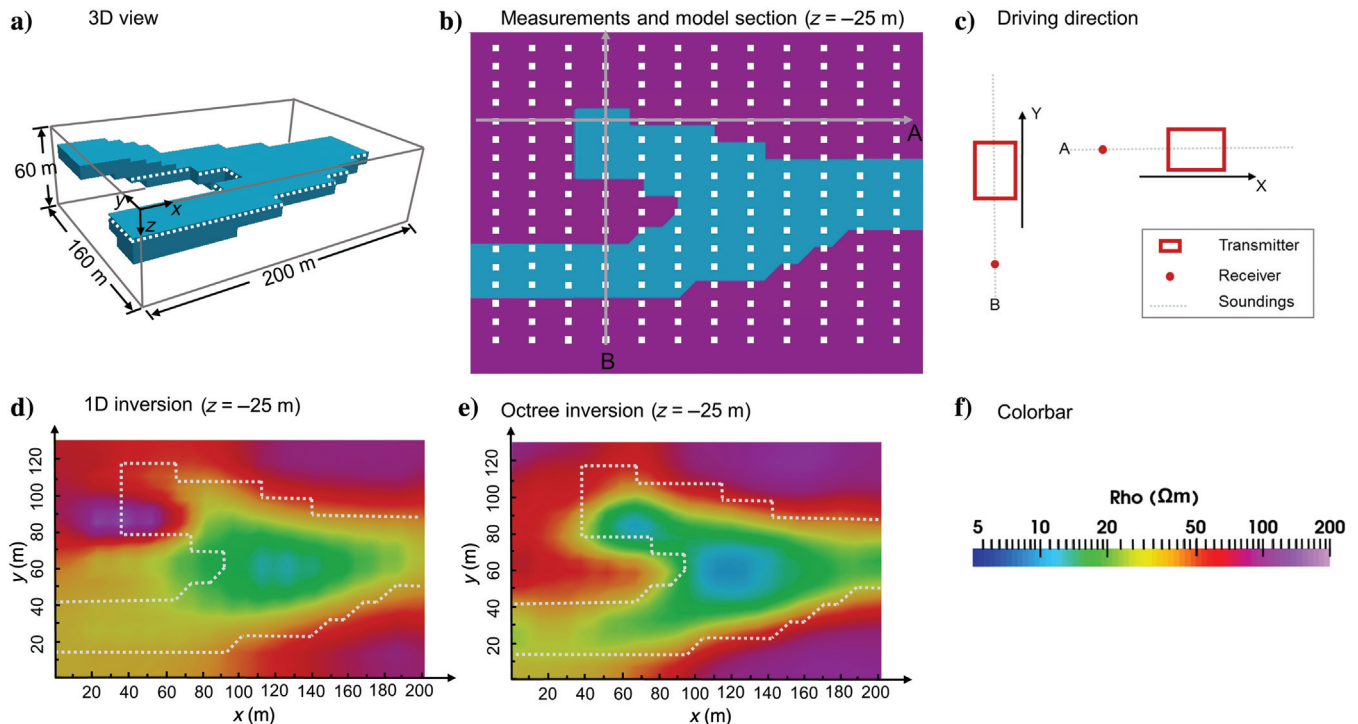


Figure 6. The 3D octree inversion for a valley model using the tTEM system. (a) A 3D view of the conductive valley, with a section plane at the depth of 25 m. (b) Soundings' layout above the valley, with 20 m distance in the  $x$ -direction and 10 m distance in the  $y$ -direction. Lines A and B are the profiles inverted in 2.5D and shown in Figure 7. (c) Two used driving directions of the tTEM system. (d) The 1D inversion result of the resistivity model section. (e) The 3D inversion result of the resistivity model section. (f) Colorbar of sections (d and e). The dotted white lines in sections (d and e) represent the extension of the valley.

tion, with strong model variations along the  $y$ -direction perpendicular to the profile, which is a violation of the 2D assumption.

In the right panels of Figure 7, profile B shows two conductive blocks (Figure 7e), i.e., the cross sections of the valley branches. Figure 7f presents a  $yz$  slice of the 3D inversion model of Figure 6 along profile B, whereas Figure 7g and 7h shows the 2.5D and 1D inversions, respectively. The 3D inversion in Figure 7f is able to image both of the branches, with better resolution on the shallower bigger branch (similarly, the deeper branch also is imaged poorer in Figure 6e). In this case, the 2.5D inversion gives good results, with good imaging of both valley branches, whereas the 1D inversion is not able to distinguish the branches, resulting in a single merged anomaly with an incorrect shape. The superior performance, in terms of model recovery, of the 2.5D inversion along profile B compared with profile A, is a direct consequence of the fact that the model is almost 2D along profile B, but highly 3D along profile A.

### FIELD EXAMPLE

Javngyde is a headwater catchment located in Jutland, Denmark, where the landscape was mainly formed during the Weichselian glaciation (Houmark-Nielsen, 2004). The general surface soil of the catchment is low-medium resistive clay-till, whereas some areas are dominated by freshwater and meltwater sandy deposits (Jakobsen et al., 2011). Some clayey glaciotectionic thrust structures are present in the area (Kim et al., 2019), and the high heterogeneity makes the site a good example to validate our 3D and 2.5D inversion algorithms. In 2017, 61% of the catchment area was surveyed with tTEM. This specific data set (see Figure 8) is a small subset of the entire data set, and it consists of 200 soundings, distributed more than nine lines oriented in a northwest-southeast direction with approximately 10 m sounding spacing along the lines and 25 m line spacing. The tTEM data were processed following the procedures described in Auken et al. (2019).

First, we performed a 3D inversion of the entire subset, and then profile L was selected for 2.5D inversion based on the 3D inverted model. Profile L holds 24 soundings. The 3D inversion of the full survey runs in 12.5 h on 10 CPUs, and the peak memory usage was 42 GB. The 2.5D inversion of profile L took 24 min and 6 GB on 12 CPUs. We also performed a 1D voxel inversion of this profile as a reference.

All of the inversions were given a homogeneous starting model of 100  $\Omega\text{m}$ . The total data misfits of the 3D full survey, the 2.5D profile, and the 1D profile are 1.2, 0.9, and 0.8, respectively.

Figure 9 presents a section of the 3D inversion model along profile L, together with the 2.5D and the 1D inversions. The depth of investigation (DOI) also is displayed in the section following (Christiansen and Auken, 2012). The misfits of the soundings along the profile are shown in Figure 9d. Overall, all of the misfits are under two, with higher misfit for the 3D inversion, which however is a part of the full survey inversion.

As shown in Figure 9, all of the inversion results have a 10 m thick medium-high resistive surface layer. According to the geology background, we interpret it as sand and gravel glacial deposits. Below 10 m, clayey glaciotectionic thrust structures are evident, but significant differences are present in the imaging of the conductive anomalies between the 1D inversion and 2.5D/3D inversions. In the northwest (left) part of the profile, the 1D inversion shows an almost

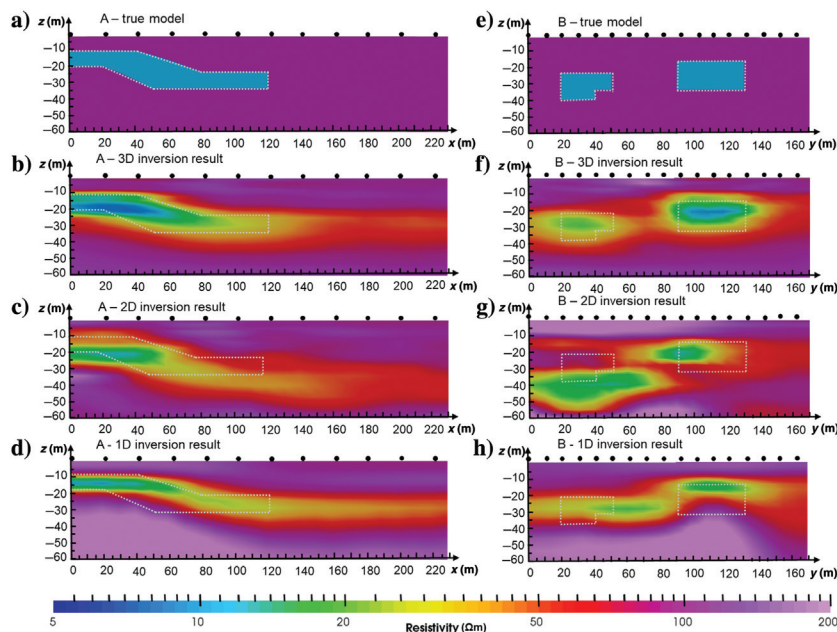


Figure 7. Model and inversion result at two profiles of the valley model. (a) True model of profile A, (b) 3D inversion result of profile A, (c) 2.5D inversion result of profile A, (d) 1D inversion result of profile A, (e) true model of profile B, (f) 3D inversion result of profile B, (g) 2.5D inversion result of profile B, and (h) 1D inversion result of profile B.

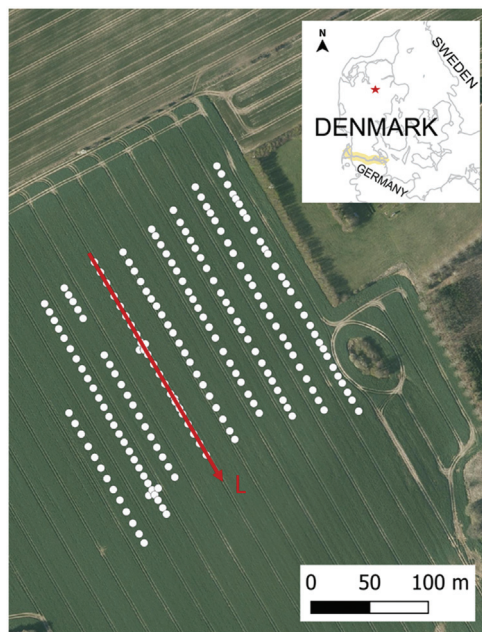


Figure 8. Map of the survey and measurement locations.

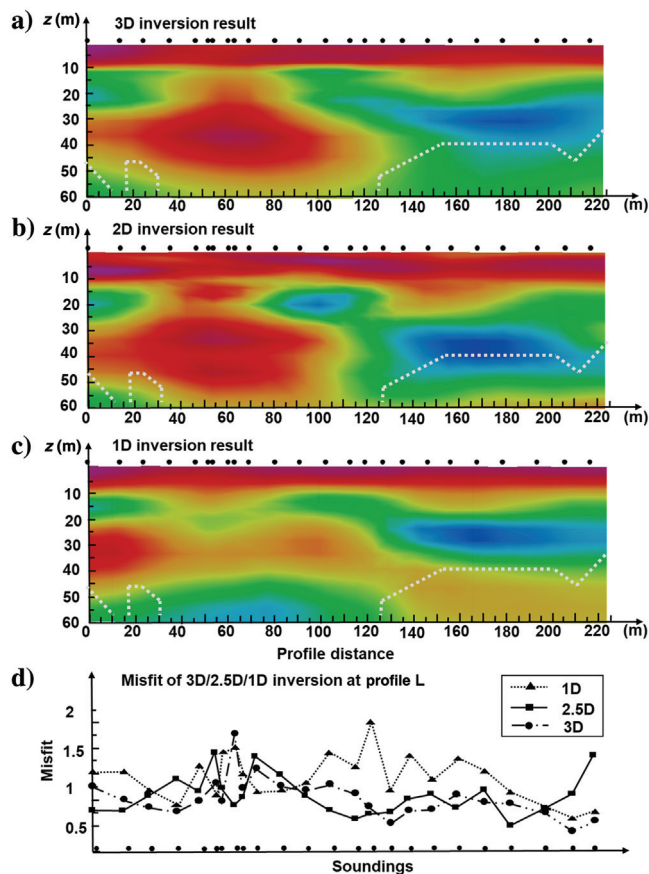


Figure 9. (a) The 3D, (b) 2.5D, (c) 1D inversion result, and (d) corresponding sounding misfit at the profile L. The dashed white lines in (a–c) represent 1D DOI.

continuous conductive anomaly at 20 m depth, contrary to the 2.5D and 3D inversions, which image two clearly distinct anomalies. Furthermore, the 1D inversion finds a deep conductive anomaly at 60 m depth, not present in the other inversions. These differences are rather similar to the ones found in the analysis of the inversions of the synthetic model of profile B in Figure 7, where the 1D inversion has a difficult time imaging the two valley branches separately. We, therefore, follow the multidimensional inversion results and interpret the southeast conductive area as a clayey thrust structure. Although the computing complexity of the 2.5D inversion is notably smaller, the inversion result is quite similar to the 3D inversion section, making it a valuable tool for inverting TEM data in complex geology, especially where the main structure directions are perpendicular to the data collection direction.

## CONCLUSION

We have presented two implementations of modeling and inversion using an octree-based FE method in 3D and 2.5D of TEM data. The octree technique offers an elegant manner to locally refine the mesh to represent geologic features and capture field variations, which reduces the degree of freedom efficiently resulting in a lower computational cost for forward modeling and Jacobian calculation. With a mirror approach, we built a 2.5D algorithm using an octree mesh, which additionally improves the efficiency of the inversion

scheme. Specifically, the 3D FE modeling using octree meshes is approximately three times faster than the tetrahedral implementations and uses only one-third of the memory. The 2.5D implementation reduces the computing time and memory use by another factor of two.

Another highlight of our implementations is the flexible link between the forward mesh and inversion model space. In particular, the 3D and 2.5D inversion models are defined in structured meshes, linked through an interpolation to the forward meshes in a domain decomposition strategy, successfully avoiding fine inversion mesh refinements without sacrificing forward accuracy.

The applicability of the proposed algorithms was demonstrated through a synthetic example with a 3D valley structure and a field example. The synthetic experiment illustrated that 3D inversion can validly recover the anomaly with the proper size and conductivity. The 2.5D inversion result approached the true model with faster speed and smaller computing expenses, as long as no strong variations in resistivity were present perpendicularly to the profile. On the contrary, the 1D inversion could not delineate the correct shape of the 3D anomaly. The field example showed good agreement between the 3D and 2.5D inversion, but with a substantial difference from a 1D inversion result. Hence, we conclude that the 3D and 2.5D octree-based inversion schemes for TEM data can resolve complicated subsurface structures. The choice between a 3D and 2.5D inversion will depend on the geologic environment and the data collection layout, but also should consider the trade-off between model resolution and computational cost.

## ACKNOWLEDGMENTS

The first author is appreciative of H. Cai for providing meaningful support on the TEM modeling program and Jacobian formula derivations. We thank P. K. Maurya for collecting and processing the field data. We appreciate A. Kass for improving the manuscript through detailed comments. The field data set was funded by the project MapField (Innovation Fund Denmark, grant no. 29771). The authors thank D. Avdeev, an anonymous reviewer, X. Garcia, and J. Etgen for their constructive comments on the manuscript.

## DATA AND MATERIALS AVAILABILITY

Data associated with this research are available and can be obtained by contacting the corresponding author.

## REFERENCES

- Abubakar, A., T. Habashy, V. Druskin, L. Knizhnerman, and D. Alumbaugh, 2008, 2.5 D forward and inverse modeling for interpreting low-frequency electromagnetic measurements: *Geophysics*, **73**, no. 4, F165–F177, doi: [10.1190/1.2937466](https://doi.org/10.1190/1.2937466).
- Allers, A., A. Sezginer, and V. L. Druskin, 1994, Solution of 2.5-dimensional problems using the Lanczos decomposition: *Radio Science*, **29**, 955–963, doi: [10.1029/94RS00828](https://doi.org/10.1029/94RS00828).
- Ansari, S., and C. G. Farquharson, 2014, 3D finite-element forward modeling of electromagnetic data using vector and scalar potentials and unstructured grids: *Geophysics*, **79**, no. 4, E149–E165, doi: [10.1190/geo2013-0172.1](https://doi.org/10.1190/geo2013-0172.1).
- Auken, E., T. Boesen, and A. V. Christiansen, 2017, A review of airborne electromagnetic methods with focus on geotechnical and hydrological applications from 2007 to 2017: *Advances in Geophysics*, **58**, 47–93, doi: [10.1016/bs.agph.2017.10.002](https://doi.org/10.1016/bs.agph.2017.10.002).
- Auken, E., and A. V. Christiansen, 2004, Layered and laterally constrained 2D inversion of resistivity data: *Geophysics*, **69**, 752–761, doi: [10.1190/1.1759461](https://doi.org/10.1190/1.1759461).

- Auken, E., A. V. Christiansen, G. Fiandaca, C. Schamper, A. A. Behroozmand, A. Binley, E. Nielsen, F. Effersø, N. B. Christensen, K. I. Sørensen, N. Foged, and G. Vignoli, 2015, An overview of a highly versatile forward and stable inverse algorithm for airborne, ground-based and borehole electromagnetic and electric data: *Exploration Geophysics*, **46**, 223–235, doi: [10.1071/EG13097](https://doi.org/10.1071/EG13097).
- Auken, E., N. Foged, J. J. Larsen, K. V. T. Lassen, P. K. Maurya, S. M. Dath, and T. T. Eiskjær, 2019, tTEM — A towed transient electromagnetic system for detailed 3D imaging of the top 70 m of the subsurface: *Geophysics*, **84**, no. 1, E13–E22, doi: [10.1190/geo2018-0355.1](https://doi.org/10.1190/geo2018-0355.1).
- Bielak, J., O. Ghattas, and E. Kim, 2005, Parallel octree-based finite element method for large-scale earthquake ground motion simulation: *Computer Modeling in Engineering and Sciences*, **10**, 99, doi: [10.3970/cmcs.2005.010.099](https://doi.org/10.3970/cmcs.2005.010.099).
- Börner, R.-U., 2010, Numerical modeling in geo-electromagnetics: Advances and challenges: *Surveys in Geophysics*, **31**, 225–245, doi: [10.1007/s10712-009-9087-x](https://doi.org/10.1007/s10712-009-9087-x).
- Brodie, R., and A. Fisher, 2008, Inversion of TEMPEST AEM survey data, Honeysuckle Creek, Victoria: Geoscience Australia for the Bureau of Rural Sciences.
- Butcher, J. C., and N. Goodwin, 2008, Numerical methods for ordinary differential equations: Wiley Online Library, 2.
- Christensen, N. B., 2014, Sensitivity functions of transient electromagnetic methods: *Geophysics*, **79**, no. 4, E167–E182, doi: [10.1190/geo2013-0364.1](https://doi.org/10.1190/geo2013-0364.1).
- Christensen, N. B., 2016, Fast approximate 1D modeling and inversion of transient electromagnetic data: *Geophysical Prospecting*, **64**, 1620–1631, doi: [10.1111/1365-2478.12373](https://doi.org/10.1111/1365-2478.12373).
- Christensen, N. K., T. P. A. Ferre, G. Fiandaca, and S. Christensen, 2017, Voxel inversion of airborne electromagnetic data for improved groundwater model construction and prediction accuracy: *Hydrology and Earth System Sciences*, **21**, 1321–1337, doi: [10.5194/hess-21-1321-2017](https://doi.org/10.5194/hess-21-1321-2017).
- Christiansen, A. V., and E. Auken, 2012, A global measure for depth of investigation: *Geophysics*, **77**, no. 4, WB171–WB177, doi: [10.1190/geo2011-0393.1](https://doi.org/10.1190/geo2011-0393.1).
- Christiansen, A. V., E. Auken, C. Kirkegaard, C. Schamper, and G. Vignoli, 2016, An efficient hybrid scheme for fast and accurate inversion of airborne transient electromagnetic data: *Exploration Geophysics*, **47**, 323–330, doi: [10.1071/EG14121](https://doi.org/10.1071/EG14121).
- Commer, M., G. M. Hoversten, and E. S. Um, 2015, Transient-electromagnetic finite-difference time-domain earth modeling over steel infrastructure: *Geophysics*, **80**, no. 2, E147–E162, doi: [10.1190/geo2014-0324.1](https://doi.org/10.1190/geo2014-0324.1).
- Cox, L. H., G. A. Wilson, and M. S. Zhdanov, 2012, 3D inversion of airborne electromagnetic data: *Geophysics*, **77**, no. 4, WB59–WB69, doi: [10.1190/geo2011-0370.1](https://doi.org/10.1190/geo2011-0370.1).
- Frey, P. J., and P.-L. George, 2007, Mesh generation: Application to finite elements: ISTE.
- Fullagar, P. K., G. A. Pears, J. E. Reid, and R. Schaa, 2015, Rapid approximate inversion of airborne TEM: *Exploration Geophysics*, **46**, 112–117, doi: [10.1071/EG14046](https://doi.org/10.1071/EG14046).
- Grayver, A. V., 2015, Parallel three-dimensional magnetotelluric inversion using adaptive finite-element method. Part I: Theory and synthetic study: *Geophysical Journal International*, **202**, 584–603, doi: [10.1093/gji/ggv165](https://doi.org/10.1093/gji/ggv165).
- Grayver, A. V., and T. V. Kolev, 2015, Large-scale 3D geoelectromagnetic modeling using parallel adaptive high-order finite element method EM modeling with high-order FEM: *Geophysics*, **80**, no. 6, E277–E291, doi: [10.1190/geo2015-0013.1](https://doi.org/10.1190/geo2015-0013.1).
- Haber, E., U. Ascher, and D. W. Oldenburg, 2002, 3D forward modeling of time domain electromagnetic data: 72nd Annual International Meeting, SEG, Expanded Abstracts, 641–644, doi: [10.1190/1.1817334](https://doi.org/10.1190/1.1817334).
- Haber, E., and S. Heldmann, 2007, An octree multigrid method for quasi-static Maxwell's equations with highly discontinuous coefficients: *Journal of Computational Physics*, **223**, 783–796, doi: [10.1016/j.jcp.2006.10.012](https://doi.org/10.1016/j.jcp.2006.10.012).
- Haber, E., and C. Schwarzbach, 2014, Parallel inversion of large-scale airborne time-domain electromagnetic data with multiple Octree meshes: *Inverse Problems*, **30**, 055011, doi: [10.1088/0266-5611/30/5/055011](https://doi.org/10.1088/0266-5611/30/5/055011).
- Hanke, M., 1997, A regularizing Levenberg-Marquardt scheme, with applications to inverse groundwater filtration problems: *Inverse Problems*, **13**, 79, doi: [10.1088/0266-5611/13/1/007](https://doi.org/10.1088/0266-5611/13/1/007).
- Horesh, L., and E. Haber, 2011, A second order discretization of Maxwell's equations in the quasi-static regime on octree grids: *SIAM Journal on Scientific Computing*, **33**, 2805–2822, doi: [10.1137/100798508](https://doi.org/10.1137/100798508).
- Houmark-Nielsen, M., 2004, The Pleistocene of Denmark: A review of stratigraphy and glaciation history: *Developments in Quaternary Sciences*, **2**, 35–46, doi: [10.1016/S1571-0866\(04\)80055-1](https://doi.org/10.1016/S1571-0866(04)80055-1).
- Jahandari, H., and C. G. Farquharson, 2014, A finite-volume solution to the geophysical electromagnetic forward problem using unstructured grids: *Geophysics*, **79**, no. 6, E287–E302, doi: [10.1190/geo2013-0312.1](https://doi.org/10.1190/geo2013-0312.1).
- Jakobsen, P. R., B. Hermansen, and L. Tougaard, 2011, Danmarks digitale Jordartskort 1: 25 000: GEUS, Geological Survey of Denmark and Greenland.
- Jin, J.-M., 2015, The finite element method in electromagnetics: John Wiley & Sons.
- Kim, H., A.-S. Høyer, R. Jakobsen, L. Thorling, J. Aamand, P. K. Maurya, A. V. Christiansen, and B. Hansen, 2019, 3D characterization of the subsurface redox architecture in complex geological settings: *Science of the Total Environment*, **693**, 133583, doi: [10.1016/j.scitotenv.2019.133583](https://doi.org/10.1016/j.scitotenv.2019.133583).
- Legrain, G., R. Allais, and P. Cartraud, 2011, On the use of the extended finite element method with quadtree/octree meshes: *International Journal for Numerical Methods in Engineering*, **86**, 717–743, doi: [10.1002/nme.3070](https://doi.org/10.1002/nme.3070).
- Madsen, L. M., G. Fiandaca, and E. Auken, 2020, 3-D time-domain spectral inversion of resistivity and full-decay induced polarization data — Full solution of Poisson's equation and modeling of the current waveform: *Geophysical Journal International*, **223**, 2101–2116, doi: [10.1093/gji/ggaa443](https://doi.org/10.1093/gji/ggaa443).
- Maurya, P. K., A. V. Christiansen, J. Pedersen, and E. Auken, 2020, High resolution 3D subsurface mapping using a towed transient electromagnetic system-tTEM: Case studies: *Near Surface Geophysics*, **18**, 249–259, doi: [10.1002/nsg.12094](https://doi.org/10.1002/nsg.12094).
- McMillan, M., E. Haber, and D. Marchant, 2018, Large scale 3D airborne electromagnetic inversion—recent technical improvements: ASEG, Expanded Abstracts, 1–6.
- Menke, W., 2018, Geophysical data analysis: Discrete inverse theory: Academic Press.
- Mitsuhata, Y., T. Uchida, and H. Amano, 2002, 2.5-D inversion of frequency-domain electromagnetic data generated by a grounded-wire source: *Geophysics*, **67**, 1753–1768, doi: [10.1190/1.1527076](https://doi.org/10.1190/1.1527076).
- Oldenburg, D. W., E. Haber, and R. Shekhtman, 2013, Three dimensional inversion of multisource time domain electromagnetic data: *Geophysics*, **78**, no. 1, E47–E57, doi: [10.1190/geo2012-0131.1](https://doi.org/10.1190/geo2012-0131.1).
- Schenk, O., and K. Gärtner, 2004, Solving unsymmetric sparse systems of linear equations with PARDISO: *Future Generation Computer Systems*, **20**, 475–487, doi: [10.1016/j.future.2003.07.011](https://doi.org/10.1016/j.future.2003.07.011).
- Schwarzbach, C., R.-U. Börner, and K. Spitzer, 2011, Three-dimensional adaptive higher order finite element simulation for geo-electromagnetics — A marine CSEM example: *Geophysical Journal International*, **187**, 63–74, doi: [10.1111/j.1365-246X.2011.05127.x](https://doi.org/10.1111/j.1365-246X.2011.05127.x).
- Um, E. S., 2011, Three-dimensional finite-element time-domain modeling of the marine controlled-source electromagnetic method: Stanford University.
- Um, E. S., J. M. Harris, and D. L. Alumbaugh, 2010, 3D time-domain simulation of electromagnetic diffusion phenomena: A finite-element electric-field approach finite-element time-domain simulation: *Geophysics*, **75**, no. 4, F115–F126, doi: [10.1190/1.3473694](https://doi.org/10.1190/1.3473694).
- Viezzoli, A., A. V. Christiansen, E. Auken, and K. Sørensen, 2008, Quasi-3D modeling of airborne TEM data by spatially constrained inversion: *Geophysics*, **73**, no. 3, F105–F113, doi: [10.1190/1.2895521](https://doi.org/10.1190/1.2895521).
- Vignoli, G., G. Fiandaca, A. V. Christiansen, C. Kirkegaard, and E. Auken, 2015, Sharp spatially constrained inversion with applications to transient electromagnetic data: *Geophysical Prospecting*, **63**, 243–255, doi: [10.1111/1365-2478.12185](https://doi.org/10.1111/1365-2478.12185).
- Wilson, G., A. Raiche, and F. Sugeng, 2006, 2.5 D inversion of airborne electromagnetic data: *Exploration Geophysics*, **37**, 363–371, doi: [10.1071/EG06363](https://doi.org/10.1071/EG06363).
- Yang, D., and D. W. Oldenburg, 2012, Three-dimensional inversion of airborne time-domain electromagnetic data with applications to a porphyry deposit: *Geophysics*, **77**, no. 2, B23–B34, doi: [10.1190/geo2011-0194.1](https://doi.org/10.1190/geo2011-0194.1).
- Yang, D., D. W. Oldenburg, and E. Haber, 2013, 3-D inversion of airborne electromagnetic data parallelized and accelerated by local mesh and adaptive soundings: *Geophysical Journal International*, **196**, 1492–1507, doi: [10.1093/gji/ggt465](https://doi.org/10.1093/gji/ggt465).
- Yu, W. W., and E. Haber, 2012, A 2.5 D inversion of airborne electromagnetic data: 82nd Annual International Meeting, SEG, Expanded Abstracts, doi: [10.1190/segam2012-0592.1](https://doi.org/10.1190/segam2012-0592.1).
- Zhang, B., E. W. Kim, F. Gianluca, H. Cai, and E. Auken, 2021, 3D inversion of time domain electromagnetic data using finite elements and a triple mesh formulation: *Geophysics*, **86**, no. 3, E257–E267, doi: [10.1190/geo2020-0079.1](https://doi.org/10.1190/geo2020-0079.1).
- Zhdanov, M. S., S. K. Lee, and K. Yoshioka, 2006, Integral equation method for 3D modeling of electromagnetic fields in complex structures with inhomogeneous background conductivity: *Geophysics*, **71**, no. 6, G333–G345, doi: [10.1190/1.2358403](https://doi.org/10.1190/1.2358403).

Biographies and photographs of the authors are not available.